

engineered. The low-loss deep-subwavelength loading structures used in RPM would be challenging or impossible to implement in optical-frequency systems, enabling a rich landscape of phase-matched nonlinear microwave circuits.

REFERENCES AND NOTES

1. S. J. Weber *et al.*, *Nature* **511**, 570–573 (2014).
2. N. Roch *et al.*, *Phys. Rev. Lett.* **112**, 170501 (2014).
3. P. Campagne-Ibarcq *et al.*, *Phys. Rev. Lett.* **112**, 180402 (2014).
4. M. Hatridge *et al.*, *Science* **339**, 178–181 (2013).
5. R. Vijay *et al.*, *Nature* **490**, 77–80 (2012).
6. G. de Lange *et al.*, *Phys. Rev. Lett.* **112**, 080501 (2014).
7. S. Shankar *et al.*, *Nature* **504**, 419–422 (2013).
8. C. Eichler, Y. Salathe, J. Mlynec, S. Schmidt, A. Wallraff, *Phys. Rev. Lett.* **113**, 110502 (2014).
9. E. Flurin, N. Roch, F. Mallet, M. H. Devoret, B. Huard, *Phys. Rev. Lett.* **109**, 183901 (2012).
10. R. Barends *et al.*, *Nature* **508**, 500–503 (2014).
11. D. Ristè *et al.*, *Nat. Commun.* **6**, 6983 (2015).
12. J. M. Chow *et al.*, *Nat. Commun.* **5**, 4015 (2014).
13. M. A. Castellanos-Beltran, K. W. Lehnert, *Appl. Phys. Lett.* **91**, 083509 (2007).
14. N. Bergeal *et al.*, *Nature* **465**, 64–68 (2010).
15. M. Hatridge, R. Vijay, D. H. Slichter, J. Clarke, I. Siddiqi, *Phys. Rev. B* **83**, 134501 (2011).
16. C. Caves, *Phys. Rev. D Part. Fields* **26**, 1817–1839 (1982).
17. T. Yamamoto *et al.*, *Appl. Phys. Lett.* **93**, 042510 (2008).
18. N. Roch *et al.*, *Phys. Rev. Lett.* **108**, 147701 (2012).
19. C. Eichler, A. Wallraff, *EPJ Quantum Technology* **1**, 2 (2014).
20. J. Y. Mutus *et al.*, *Appl. Phys. Lett.* **104**, 263513 (2014).
21. K. O'Brien, C. Macklin, I. Siddiqi, X. Zhang, *Phys. Rev. Lett.* **113**, 157001 (2014).
22. B. Ho Eom, P. K. Day, H. G. LeDuc, J. Zmuidzinas, *Nat. Phys.* **8**, 623–627 (2012).
23. C. Bockstiegel *et al.*, *J. Low Temp. Phys.* **176**, 476–482 (2014).
24. S. K. Tolpygo *et al.*, *IEEE Trans. Appl. Supercond.* **25**, 1101312 (2015).
25. Materials and methods are available as supplementary materials on Science Online.
26. G. P. Agrawal, *Nonlinear Fiber Optics* (Academic Press, Oxford, ed. 5, 2013).
27. A. Blais, R.-S. Huang, A. Wallraff, S. M. Girvin, R. J. Schoelkopf, *Phys. Rev. A* **69**, 062320 (2004).
28. J. E. Fernandez, "A Noise Measurement System Using a Cryogenic Attenuator," *TMO Prog. Rep.* **42-135** (1998).
29. L. Spietz, K. W. Lehnert, I. Siddiqi, R. J. Schoelkopf, *Science* **300**, 1929–1932 (2003).
30. M. A. Castellanos-Beltran, K. D. Irwin, G. C. Hilton, L. R. Vale, K. W. Lehnert, *Nat. Phys.* **4**, 929–931 (2008).
31. H. Paik *et al.*, *Phys. Rev. Lett.* **107**, 240501 (2011).
32. M. Boissonneault, J. M. Gambetta, A. Blais, *Phys. Rev. A* **79**, 013819 (2009).
33. A. Korotkov, *Phys. Rev. B* **63**, 115403 (2001).
34. J. E. Johnson *et al.*, *Phys. Rev. Lett.* **109**, 050506 (2012).

ACKNOWLEDGMENTS

We acknowledge A. Kamal, S. Tolpygo, and G. Fitch for useful discussions and technical assistance. C.M. acknowledges E. Hassell and J. Luke for useful discussions. This research is based on work supported in part by the Army Research Office (under grant no. W911NF-14-1-0078); the Office of the Director of National Intelligence (ODNI), Intelligence Advanced Research Projects Activity (IARPA), via MIT Lincoln Laboratory under Air Force Contract FA8721-05-C-0002; and a Multidisciplinary University Research Initiative from the Air Force Office of Scientific Research MURI grant no. FA9550-12-1-0488. The views and conclusions contained herein are those of the authors and should not be interpreted as necessarily representing the official policies or endorsements, either expressed or implied, of ODNI, IARPA, or the U.S. government. The U.S. government is authorized to reproduce and distribute reprints for governmental purpose notwithstanding any copyright annotation thereon. M.E.S. acknowledges support from a Hertz Foundation Fellowship.

SUPPLEMENTARY MATERIALS

www.sciencemag.org/content/350/6258/307/suppl/DC1
Materials and Methods
Figs. S1 to S12

5 February 2015; accepted 19 August 2015
Published online 3 September 2015
10.1126/science.aaa8525

OCEANOGRAPHY

Sensitivity of seafloor bathymetry to climate-driven fluctuations in mid-ocean ridge magma supply

J.-A. Olive,^{1*} M. D. Behn,² G. Ito,³ W. R. Buck,¹ J. Escartin,⁴ S. Howell³

Recent studies have proposed that the bathymetric fabric of the seafloor formed at mid-ocean ridges records rapid (23,000 to 100,000 years) fluctuations in ridge magma supply caused by sea level changes that modulate melt production in the underlying mantle. Using quantitative models of faulting and magma emplacement, we demonstrate that, in fact, seafloor-shaping processes act as a low-pass filter on variations in magma supply, strongly damping fluctuations shorter than about 100,000 years. We show that the systematic decrease in dominant seafloor wavelengths with increasing spreading rate is best explained by a model of fault growth and abandonment under a steady magma input. This provides a robust framework for deciphering the footprint of mantle melting in the fabric of abyssal hills, the most common topographic feature on Earth.

Seafloor abyssal hills are the most common topographic feature on the surface of the solid Earth. They consist of a juxtaposition of bathymetric highs and lows with a characteristic spacing of 1 to 10 km and amplitude of up to a few hundred meters, elongated parallel to crustal isochrons (1–3). These features form at mid-ocean ridges (MORs) through the interaction of

volcanism and faulting coincident with the creation of new oceanic lithosphere (2, 4, 5) (Fig. 1).

The fabric of abyssal hills has recently been proposed to record fluctuations in MOR magma supply driven by climatically controlled sea level variations with a periodicity of up to 100 thousand years (ky) (6). It was shown that sea level changes of ~100 m associated with glacial (Milankovitch) cycles could induce pressure changes on the subridge mantle undergoing decompression melting, thereby modulating the flux of melt supplied to the ridge axis (6, 7). This mechanism was proposed to drive oceanic crustal thickness

¹Lamont-Doherty Earth Observatory, Columbia University, Palisades NY, USA. ²Woods Hole Oceanographic Institution, Woods Hole MA, USA. ³University of Hawaii, Honolulu HI, USA. ⁴CNRS, Institut de Physique du Globe de Paris, Paris, France.
*Corresponding author. E-mail: jaolive@ldeo.columbia.edu

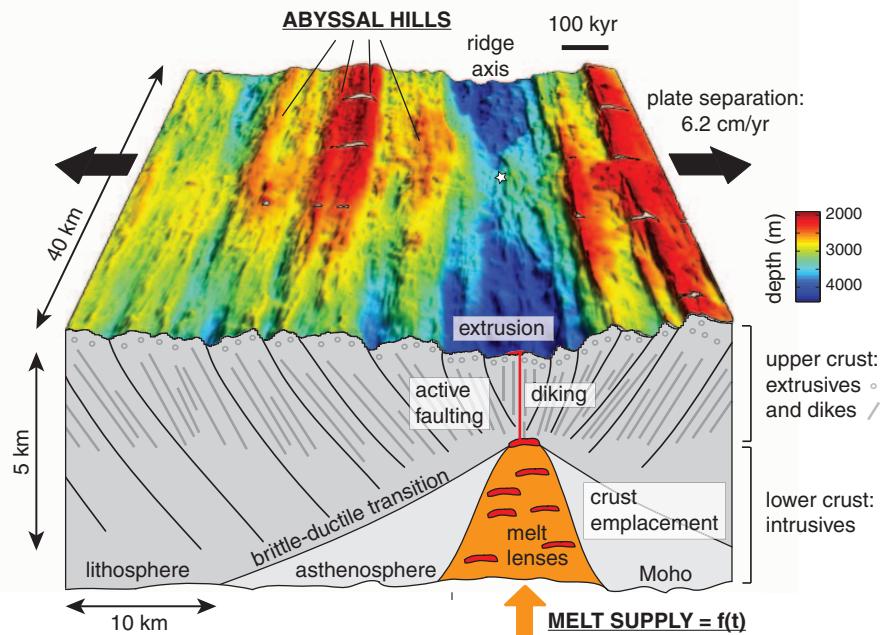


Fig. 1. Abyssal hill fabric formed at the intermediate-spreading Chile Ridge. Bathymetry of a segment of the intermediate-spreading Chile Ridge (29) located at 39°12'S, 91°30'W (white star), looking south. Beneath is a schematic cross section showing the major tectono-magmatic processes that shape the seafloor as melt supplied from below is emplaced as new oceanic crust.

fluctuations of ~600 m and give rise to isostatically compensated seafloor topography with wavelengths reflecting Milankovitch periodicities (23, 41, and 100 ky). Spectral power at these wavelengths in the bathymetry of the intermediate-spreading Australian-Antarctic Ridge (AAR) was presented as evidence for this process (6). Moreover, an independent study revealed a strong spectral peak near the 100-ky period for seafloor created at the fast-spreading East Pacific Rise, although peaks at the 23- and 41-ky periods were not observed (8). If confirmed, a major implication of this model is that abyssal hill fabric represents a proxy for paleo sea-level change.

Climate-driven changes in magma supply in several terrestrial settings have been attributed to the loss of glaciers, some up to 2 km thick (9, 10). However, whether ~100-m change in sea level can be effectively recorded in seafloor bathymetry is unclear (6, 7, 11). We combine classic seafloor observations with recently developed and improved models of MOR dynamics to determine whether oscillations in melt supply of a given period (τ) can imprint seafloor bathymetry through three mechanisms: (i) static topographic compensation, (ii) volcanic extrusion on the seafloor, and (iii) tectonomagmatic interactions during normal fault growth.

The first mechanism linking MOR magma supply and seafloor bathymetry is (i) temporal (and hence cross-axis) oscillations in crustal thickness, applying a vertical load on the oceanic lithosphere that can deflect the seafloor (6). The

wavelength of the load ($U \times \tau$, where U is the spreading half-rate) strongly controls the response of the lithosphere, which is commonly described as the flexing of a thin elastic plate of effective thickness T_e (12, 13) (Fig. 2A). Because ~70% of the entire crust at intermediate- and fast-spreading ridges accretes as intrusive lower crust (14), fluctuations in melt supply will be expressed primarily as vertical undulations of the crust-mantle interface loading the lithosphere from below. In (6), however, flexure was ignored in favor of an Airy isostasy approximation. This yielded variations in seafloor topography of ~150 m in response to 600-m variations in crustal thickness driven by sea level changes over a range of spreading rates. This approximation is valid when $U \times \tau$ is greater than ~100 T_e , but this is not likely to be the case in general.

At slow-spreading ridges, Milankovitch cycles would create crustal loads of wavelength <3 km, which is considerably less than 10 T_e , as T_e has been shown to be greater than ~1 km (13, 15). Such loads should result in essentially no seafloor topography (Fig. 2A). By contrast, T_e is likely to be minimal at fast-spreading ridges, such as the East Pacific Rise, where the observed rise crest topography is best explained by a T_e of 100 m at the axis, although it thickens rapidly with lithosphere age to reach ~800 m in 100-ky-old lithosphere (16). A value of $T_e = 100$ m could explain topographic variations of ~70 to 110 m at the wavelength corresponding to the longest Milankovitch period (i.e., 8 km for $U = 8$ cm/year, assuming average

crustal densities between 2850 and 3000 kg m^{-3}). However, this estimate drops to ~5 m when using a value of T_e averaged over the wavelength of the load ($T_e = 500$ m) (Fig. 2A). Finally, at the AAR ($U = 3$ cm/year), creating seafloor topography greater than 10 m would require a $T_e \leq 100$ m, unrealistically low for an intermediate-spreading ridge. In short, the lithosphere most often constitutes a strong topographic filter to such short wavelength oscillations in crustal thickness.

Yet, another consideration suggests that a ~600-m variation in crustal thickness is an overestimate. Namely, magma arising out of the mantle is delivered to a magma storage (accretion) region of finite width within the crust, before solidifying in a neovolcanic zone of comparable width (17, 18) (Fig. 1). If the melt input (volume per unit time per unit length of ridge) fluctuates by an amount $\Delta\Phi_0$ on a period shorter than its characteristic residence time in the accretion zone, these oscillations will generate crustal thickness variations that are reduced compared to estimates that assume an infinitesimally narrow accretion zone [$\Delta h_0 = \Delta\Phi_0 / 2U \sim 600$ m, as in (6)]. For example, simple mass balance arguments (12) predict that an intermediate-spreading ridge such as the AAR with a characteristic accretion zone width of 1 km would more realistically produce crustal thickness oscillations of ~410, 220, and 120 m on Milankovitch periods of 100, 41, and 23 ky, respectively (Fig. 2B). However, again at slow-to-intermediate spreading

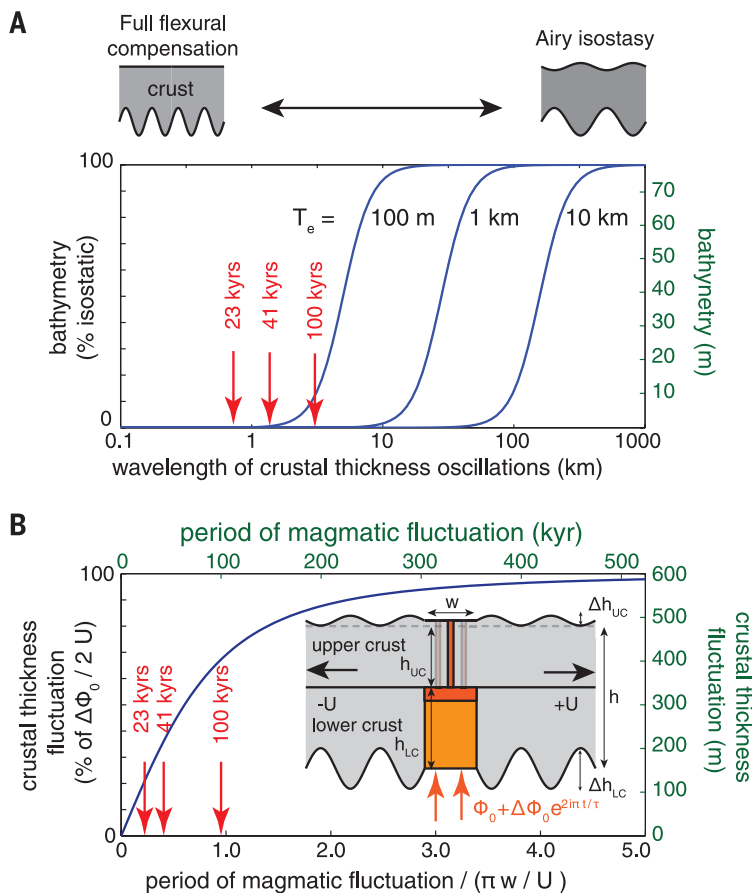


Fig. 2. Seafloor topography from static compensation mechanisms. (A) Bathymetric relief created in response to oscillations in crustal thickness on a given wavelength, assuming three different effective elastic thicknesses (T_e) for the lithosphere. Relief amplitude is given in percentage of the isostatic end-member (black axis) and in meters, assuming a crustal thickness fluctuation of 600 m and a density of 3000 kg m^{-3} for the oceanic crust (green axis). Red arrows indicate the seafloor wavelengths corresponding to Milankovitch periods for a spreading half-rate $U = 3$ cm/year. (B) Crustal thickness fluctuation ($\Delta h = \Delta h_{uc} + \Delta h_{lc}$) resulting from emplacement of a melt flux oscillating by $\Delta\Phi_0$ within a zone of width w , on a period τ . Green axes (dimensional) illustrate the case where $U = 3$ cm/year and $w = 1$ km. Black axes are normalized.

Fig. 3. A tectono-magmatic interaction model for the spacing of abyssal hills.

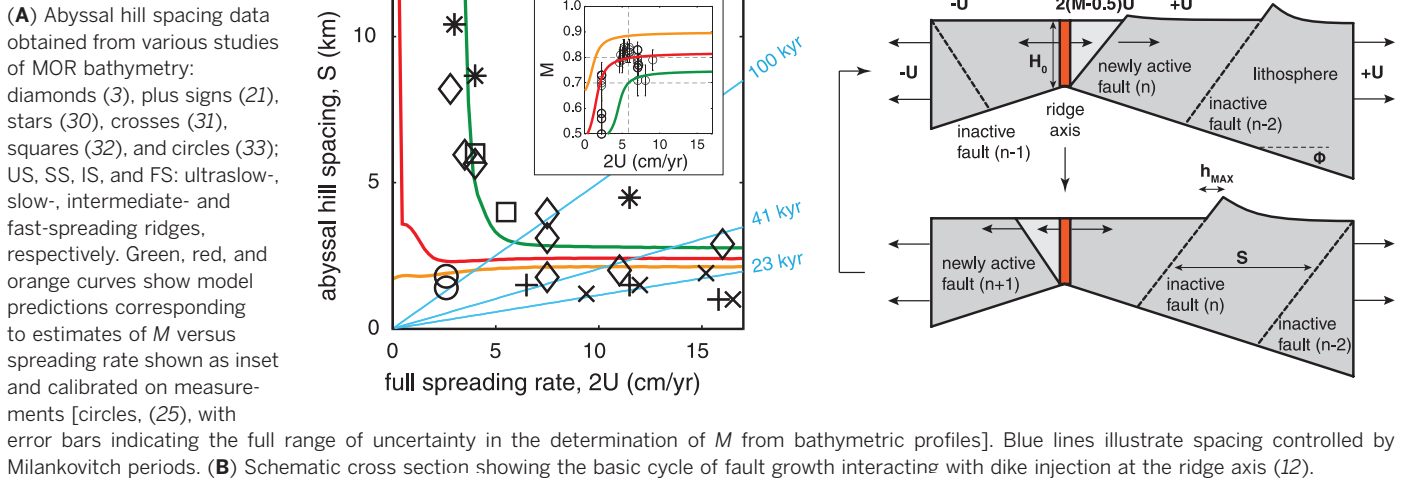
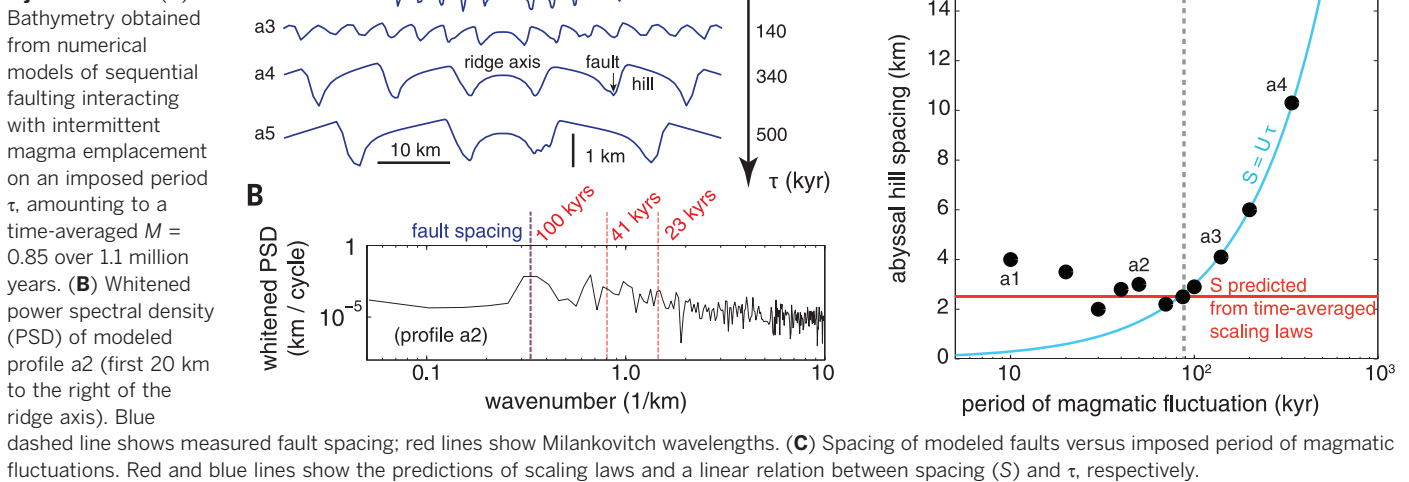


Fig. 4. Sensitivity of MOR bathymetry to fluctuating dike injection rates. (A)



rates, lithospheric flexure should drastically impede any topographic expression of these reduced thickness oscillations. At the fast-spreading East Pacific Rise ($U = 8$ cm/year), seismic evidence points to a characteristic accretion width of ~ 5 km (19). This would reduce both the estimated 100-ky crustal thickness variation and its topographic expression by a factor of 0.45, enabling at most 30 to 50 m of topography for the lowest estimate of lithospheric strength ($T_e = 100$ m).

The second mechanism for generating topography in response to oscillations in magma supply considers (ii) the portion added to the extrusive upper crust. The time-averaged volume of extruded material is thought to reflect the overpressure in an axial melt lens pushing magma upward to the seafloor (20). When transitioning from a period of thin to thick axial crust due to a change in melt supply, the overpressure must increase to compensate the replacement of dense mantle by lighter lower crust. This assumption (12) is different from

that of isostatic or flexural equilibrium explored earlier, because a column of magma rising to the surface is mechanically decoupled from the rest of the lithosphere. We can use it to estimate the thickness variation of the extrusive portion of the crust Δh_{UC} that results from the crustal thickness variations $\Delta h = 410, 220,$ and 120 m expected at the AAR (Fig. 2B). This yields $\Delta h_{UC} = 60$ to $85, 33$ to $46,$ and 18 to 25 m, respectively, depending on the density assumed for the oceanic crust. A similar reasoning predicts topographic fluctuations of 40 to 55 m on a 100-ky period at the East Pacific Rise. They are, however, unlikely to strongly overprint the tectonic fabric of the seafloor, which typically consists of fault scarps greater than 200 m at slow and intermediate-spreading ridges (3) and about 50 to 100 m at fast-spreading ridges (21). Moreover, these amplitudes are probably upper bounds, because seafloor eruptions involve lava flows spreading up to a few km in the cross-axis direction (22), providing another topographic damping process.

An important corollary to both of the above mechanisms (i and ii) is that the wavelength of the sea level–modulated topography should increase in proportion to spreading rate. However, the spacing of abyssal hills, which constitutes the dominant wavelength in the spectrum of the seafloor (23), is observed to decrease with increasing spreading rate from ~ 10 km at slow-spreading ridges down to ~ 2 km at fast-spreading ridges (Fig. 3A). Thus, any viable model for abyssal hill formation must explain this global trend.

Given that abyssal hills are typically bounded by major normal faults (2), we favor an alternative model in which the decrease in abyssal hill spacing reflects the increasing importance of magmatically versus tectonically accommodated extension at faster-spreading ridges (24). With this framework, we explore the possibility that (iii) a fluctuating magma supply influences the pattern of faulting, which shapes the seafloor fabric.

In a time-averaged sense, dike intrusion in the axial lithosphere accommodates a fraction

M of the total plate separation (Fig. 3B). The remaining fraction ($1 - M$) is accommodated by slip on normal faults that initiate near the axis and are subsequently pushed off-axis by magmatic intrusion at a rate that increases with M (24, 25). As a fault encounters progressively thicker off-axis lithosphere, the work required to keep it active increases until it becomes mechanically favorable to abandon it in favor of a new fault forming closer to the axis (Fig. 3B). Mechanical scaling laws (12) predict that thick or rapidly thickening lithosphere with a robust magma supply (high M) produces relatively short-lived, and therefore closely spaced, faults (24, 25). Upon parameterizing axial lithospheric thickness, thickening rate, and M , versus spreading rate through empirical fits to observations (Fig. 3A, inset, and fig. S2), we use these mechanical scaling laws to predict a decrease in abyssal hill spacing from ~ 10 to ~ 2.5 km with increasing spreading rate, following the trend of the observations (Fig. 3A). Thus, the systematic variations in abyssal hill fabric with spreading rate are best explained by a model of tectono-magmatic extension under a steady magma input.

Steady magma input is an oversimplification of the ridge magmatic system, even without climatic variations in magma flux (26, 27). Thus, we consider the possibility that an oscillating magma input could alter the above behavior by directly affecting the duration that individual faults remain active (28), and therefore imprint the seafloor fabric. We performed two-dimensional numerical simulations of normal fault growth coupled with magmatic injection in the lithosphere that fluctuates on a period τ (12). During 85% of the cycle, magma injection accommodates 100% of plate separation ($U = 3$ cm/year), whereas during the remaining 15%, extension is fully accommodated on faults that form spontaneously in the lithosphere. This scenario maximizes the effects of magmatic modulation but has a time-averaged M equal to 0.85 (28).

We ran 12 simulations with τ ranging from 10 to 500 ky. The modeled seafloor shows abyssal hill-like topography, from which we measure the mean fault spacing (Fig. 4A). The spectrum of topography clearly shows that fault spacing expresses a dominant wavelength (Fig. 4B). It also reveals a number of peaks at higher wave numbers (within the Milankovitch range) that cannot be directly interpreted in terms of seafloor length scales. Simulations with short τ consistently produce abyssal hills with a characteristic spacing of ~ 2 to 4 km, as predicted by the mechanical scaling laws that assume a steady magma input (horizontal red line in Fig. 4C). Simulations with a longer τ , however, reveal a direct control of the forcing period on fault spacing (blue curve). The transition between the two regimes occurs at a period set by the mechanically controlled fault spacing divided by the spreading half-rate, which at intermediate-spreading ridges is ~ 100 ky. We therefore expect the tectonic fabric of the AAR to be insensitive to even extreme fluctuations in melt supply on Milankovitch frequencies. The spectral peaks observed there (6) likely reflect only the

mechanically controlled spacing of fault-bounded abyssal hills as shaped by the time-averaged melt supply ($M \sim 0.85$) (Figs. 3A and 4B).

Each of the three mechanisms of topography development acts as a low-pass filter of melt supply with strong damping of periods shorter than ~ 100 ky. Therefore, the fingerprints of a climate modulation in MOR melt supply may be found more easily through multichannel seismic imaging of the crust-mantle boundary than through bathymetric analysis. If short-wavelength topography on the base of the crust is observed, comparing its spectral characteristics in crust younger and older than the onset of pronounced glacial cycles would provide a valuable test of the predictions made here and by earlier studies (6–8).

REFERENCES AND NOTES

1. H. Menard, J. Mammerrickx, *Earth Planet. Sci. Lett.* **2**, 465–472 (1967).
2. K. C. Macdonald, P. J. Fox, R. T. Alexander, R. Pockalny, P. Gente, *Nature* **380**, 125–129 (1996).
3. J. A. Goff, Y. Ma, A. Shah, J. R. Cochran, J.-C. Sempéré, *J. Geophys. Res.* **102**, 15521–15534 (1997).
4. D. K. Rea, *Geology* **3**, 77–80 (1975).
5. E. S. Kappel, W. B. F. Ryan, *J. Geophys. Res.* **91**, 13925–13940 (1986).
6. J. W. Crowley, R. F. Katz, P. Huybers, C. H. Langmuir, S. H. Park, *Science* **347**, 1237–1240 (2015).
7. D. C. Lund, P. D. Asimow, *Geochem. Geophys. Geosyst.* **12**, 12009 (2011).
8. M. Tolstoy, *Geophys. Res. Lett.* **42**, 1346–1351 (2015).
9. M. Nakada, H. Yokose, *Tectonophysics* **212**, 321–329 (1992).
10. M. Jull, D. McKenzie, *J. Geophys. Res.* **101**, 21815–21828 (1996).
11. P. J. Huybers, C. H. Langmuir, *Earth Planet. Sci. Lett.* **286**, 479–491 (2009).
12. Materials and methods are available as supplementary materials on Science Online.
13. A. B. Watts, *Isostasy and Flexure of the Lithosphere* (Cambridge Univ. Press, Cambridge, 2001).
14. J. P. Morgan, Y. J. Chen, *J. Geophys. Res.* **98**, 6283–6297 (1993).
15. J. R. Cochran, *J. Geophys. Res.* **84**, 4713 (1979).
16. B.-Y. Kuo, D. W. Forsyth, E. M. Parmentier, *Geophys. Res. Lett.* **13**, 681–684 (1986).
17. J. M. Sinton, R. S. Detrick, *J. Geophys. Res.* **97**, 197–216 (1992).
18. M. R. Perfit, W. W. J. Chadwick, in *Faulting and Magmatism at Mid-Ocean Ridges*, W. R. Buck et al., Eds. (AGU, Washington DC, 1998), pp. 59–115.
19. R. A. Dunn, D. R. Toomey, *Nature* **388**, 259–262 (1997).
20. W. R. Buck, S. M. Carbotte, C. Z. Mutter, *Geology* **25**, 935–938 (1997).
21. S. M. Carbotte, K. C. Macdonald, *J. Geophys. Res.* **99**, 13609–13633 (1994).
22. J. Escartin et al., *Geochem. Geophys. Geosyst.* **8**, Q06005 (2007).
23. J. A. Goff, T. H. Jordan, *J. Geophys. Res.* **93**, 13589–13608 (1988).
24. W. R. Buck, L. L. Lavier, A. N. B. Poliakov, *Nature* **434**, 719–723 (2005).
25. M. D. Behn, G. Ito, *Geochem. Geophys. Geosyst.* **9**, Q08010 (2008).
26. J. P. Canales, J. A. Collins, J. Escartin, R. S. Detrick, *J. Geophys. Res.* **105**, 28411–28425 (2000).
27. E. Bonatti et al., *Nature* **423**, 499–505 (2003).
28. G. Ito, M. D. Behn, *Geochem. Geophys. Geosyst.* **9**, Q09012 (2008).
29. J. Karsten et al., *Intern. Ridge-Crest Res.* **8**, 15–21 (1999).
30. A. Malinverno, R. A. Pockalny, *Earth Planet. Sci. Lett.* **99**, 154–169 (1990).
31. P. A. Cowie, A. Malinverno, W. B. F. Ryan, M. H. Edwards, *J. Geophys. Res.* **99**, 15205–15218 (1994).
32. A. Macario et al., *J. Geophys. Res.* **99**, 17921–17934 (1994).
33. J. Escartin et al., *J. Geophys. Res.* **104**, 10421–10437 (1999).

ACKNOWLEDGMENTS

This work greatly benefited from discussions with P. Canales, A. Soule, S. Carbotte, R. Katz, P. Huybers, and B. Ryan, as well as the constructive feedback from three anonymous reviewers. Funding was provided by NSF grants OCE-1154238 (J.-A.O. and M.D.B.), OCE-1155098 (G.I. and S.H.), EAR-1009839 (W.R.B.), CNRS support to J.E., a Woods Hole Oceanographic Institution IR&D award to M.D.B., and a Lamont-Doherty Earth Observatory Postdoctoral Fellowship for J.-A.O. The data and model results presented here are included or fully referenced in the supplementary materials.

SUPPLEMENTARY MATERIALS

www.sciencemag.org/content/350/6258/310/suppl/DC1
Materials and Methods
Figs. S1 and S2
References (34–44)

22 July 2015; accepted 3 September 2015
10.1126/science.aad0715

BIOMATERIALS

A skin-inspired organic digital mechanoreceptor

Benjamin C.-K. Tee,^{1*} Alex Chortos,^{2*} Andre Berndt,^{3*} Amanda Kim Nguyen,¹ Ariane Tom,³ Allister McGuire,⁴ Ziliang Carter Lin,⁴ Kevin Tien,¹ Won-Gyu Bae,⁵ Huiliang Wang,² Ping Mei,⁶ Ho-Hsiu Chou,⁵ Bianxiao Cui,⁴ Karl Deisseroth,³ Tse Nga Ng,^{6†} Zhenan Bao^{5†}

Human skin relies on cutaneous receptors that output digital signals for tactile sensing in which the intensity of stimulation is converted to a series of voltage pulses. We present a power-efficient skin-inspired mechanoreceptor with a flexible organic transistor circuit that transduces pressure into digital frequency signals directly. The output frequency ranges between 0 and 200 hertz, with a sublinear response to increasing force stimuli that mimics slow-adapting skin mechanoreceptors. The output of the sensors was further used to stimulate optogenetically engineered mouse somatosensory neurons of mouse cortex *in vitro*, achieving stimulated pulses in accordance with pressure levels. This work represents a step toward the design and use of large-area organic electronic skins with neural-integrated touch feedback for replacement limbs.

Neurally controlled prosthetic devices improve mobility and independence for disabled people (1). The addition of tactile sensing can benefit the utility of these neuroprosthetics by enhancing motor control

(2–4) and relieving phantom limb pain associated with limb loss (5, 6). Thus, the implementation of human mechanoreceptor-like sensing systems would be an important step toward highly functional prosthetics.

This copy is for your personal, non-commercial use only.

If you wish to distribute this article to others, you can order high-quality copies for your colleagues, clients, or customers by [clicking here](#).

Permission to republish or repurpose articles or portions of articles can be obtained by following the guidelines [here](#).

The following resources related to this article are available online at www.sciencemag.org (this information is current as of October 15, 2015):

Updated information and services, including high-resolution figures, can be found in the online version of this article at:

<http://www.sciencemag.org/content/350/6258/310.full.html>

Supporting Online Material can be found at:

<http://www.sciencemag.org/content/suppl/2015/10/14/350.6258.310.DC1.html>

This article **cites 40 articles**, 7 of which can be accessed free:

<http://www.sciencemag.org/content/350/6258/310.full.html#ref-list-1>

This article appears in the following **subject collections**:

Geochemistry, Geophysics

http://www.sciencemag.org/cgi/collection/geochem_phys